

Illumination-Invariant Active Camera Relocalization for Fine-Grained Change Detection in the Wild

Nan Li^{1,2} · Wei Feng^{1,2}✉ · Qian Zhang^{1,2}

the date of receipt and acceptance should be inserted later

Abstract Active camera relocalization (ACR) is a new problem in computer vision that significantly reduces the false alarm caused by image distortions due to camera pose misalignment in fine-grained change detection (FGCD). Despite the fruitful achievements that ACR can support, it still remains a challenging problem caused by the unstable results of relative pose estimation, especially for outdoor scenes, where the lighting condition is out of control, i.e., the twice observations may have highly varied illuminations. This paper studies an illumination-invariant active camera relocalization method, it improves both in relative pose estimation and scale estimation. We use plane segments as an intermediate representation to facilitate feature matching, thus further boosting pose estimation robustness and reliability under lighting variances. Moreover, we construct a linear system to obtain the absolute scale in each ACR iteration by minimizing the image warping error, thus, significantly reduce the time consume of ACR process, it is nearly 1.6 times faster than the state-of-the-art ACR strategy. Our work greatly expands the feasibility of real-world fine-grained change monitoring

tasks for cultural heritages. Extensive experiments tests and real-world applications verify the effectiveness and robustness of the proposed pose estimation method using for ACR tasks.

Keywords Active camera relocalization, relative pose estimation, illumination invariance

1 Introduction

Active camera relocalization (ACR) is a new but classical problem in computer vision, it physically and precisely relocates the current camera to the same pose of the reference one, by actively adjusting the camera pose (Tian et al., 2018). This approach that physical align observations is designed to support the Fine-grained change detection (FGCD) task, it aims to detect very fine-grained changes between high-value scenes over long intervals. To guarantee the faithfulness of FGCD results and avoid false alarms caused by distortion from the image alignment algorithm (Shotton et al., 2013; Guzman-Rivera et al., 2014), we need to obtain highly consistent image observations between two collections via ACR process. Hence the relocalization precision of ACR is very important, which indeed relies on the accuracy of relative camera pose estimation. As shown in Fig 1, even if the difference between two observations is only 0.5° , it still harm the authenticity of detected fine-grained changes.

For real-world ACR problems, both accuracy and robustness of pose estimation are critical, especially for outdoor scenes with large illumination change. Despite existing ACR strategies (Feng et al., 2016; Tian et al., 2018; Miao et al., 2018) work well in indoor scenes, it cannot work well in outdoor scenes where lighting condition is fully out of control, e.g., cultural heritages or

Nan Li
E-mail: linan94@tju.edu.cn

Wei Feng ✉(corresponding author)
E-mail: wfeng@tju.edu.cn

Qian Zhang
E-mail: qianz@tju.edu.cn

¹ The College of Intelligence and Computing, Tianjin University, Tianjin, China.

² The Key Research Center for Surface Monitoring and Analysis of Cultural Relics (SMARC), State Administration of Cultural Heritage, China.

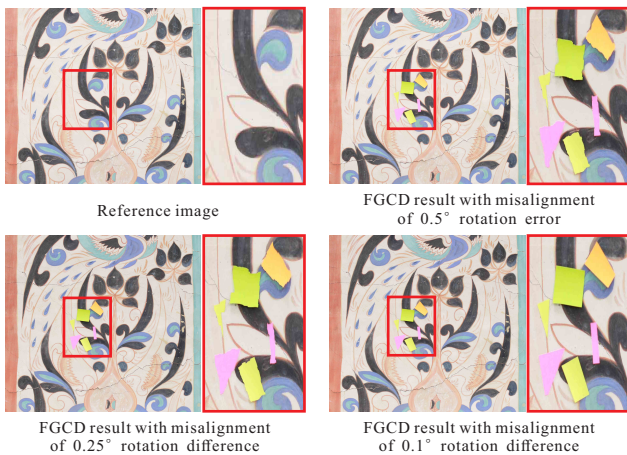


Fig. 1: The effect of images’ physical alignment on FGCD results. The real man-made fine-grained changes are regular geometries. When there is a deviation greater than 0.1° between the two images, the FGCD algorithm contorts those changes to irregular shapes. Note the camera is 50 centimeters away from the object, which is the parameter we use in actual work.

vital equipment in the wild. This is mainly due to the straightforward SIFT or other traditional image feature matching throughout the whole image domain. It results in insufficient and unreliable point correspondences under large illumination change, thus further harming the accuracy of the pose estimation results.

With the rapid development and impressive success of deep learning, researchers recently utilized convolutional neural networks for relative pose estimation problems. One approach is to learn to predict the relative pose between images (Ummenhofer et al., 2017; Balntas et al., 2018; Laskar et al., 2017), the second type is to train models for interest point detectors and descriptors fit for multiple-view feature matching (DeTone et al., 2018; Dusmanu et al., 2019; Yi et al., 2016). As evaluated in (Sattler et al., 2019), such data-driven approaches, though, may alleviate the adverse effect of illumination change problems to some extent, yield less accurate results compared to the traditional 3D structure-based methods. Moreover, the generalization capability of learning-based method is highly correlated with the training data or limited on some specific scenes, whose performance, however, is not satisfactory on various real-world scenes.

Therefore, an urgent and challenging requirement is how to obtain reliable and stable ACR results under the complexity and unrestricted environment in the wild, that is, the lighting condition is fully not of control. To this end, we need to estimate the relative pose as accurately as possible under such conditions. In addition,

due to the lack of absolute motion scale in pose estimation, the state-of-the-art ACR methods (Feng et al., 2016; Tian et al., 2018) rely on iterative adjustments, such as bisection approaches, by guessing the motion scale and gradually reducing it to approach the target camera pose. Such a guessing process harms the efficiency of ACR process.

In this paper, we propose an illumination-invariant active camera relocalization method (i^2 ACR) to eliminate the drawbacks discussed above. Firstly, based on a known physical robotic motion in an initialization module, we construct a linear system to obtain the absolute motion scale in each ACR iteration by minimizing the image warping error. Secondly, image features like SIFT reflect the local gradient distribution of the image. For the planar region in the image, lighting changes will change the pixel value but has a limited influence on the gradient distribution. Thus, for each image pair requested to estimate relative camera pose, we extract the plane regions from the two images, respectively. After that, we use plane segments as an intermediate representation to facilitate feature matching, thus further boosting pose estimation robustness under lighting changes, while maintaining high accuracy.

Our contributions are as follows: 1) We present a fast and robust ACR algorithm i^2 ACR, it performs faster than the state-of-the-art ACR strategy and shows superior performance under scenes with large illumination. 3) We conduct extensive experiments to verify the feasibility and efficiency of the proposed method. Our approach extends the ACR to more tough real-world scenes, greatly promotes the preventive conservation of cultural heritages in the wild environment.

2 Related Work

2.1 Active Camera Relocalization

Active camera relocalization, a critical step in the fine-grained change detection task (Feng et al., 2015), is proposed to overcome the image distortion caused by the virtual image alignment (Tian et al., 2018). Unlike Active recurrence of lighting (ALR), which is used to actively reproduce the lighting conditions of the rephotograph (Zhang et al., 2018), ACR employs a mechanical platform to physically adjust the camera itself to return to the position in which the reference image was taken. So far, ACR has been widely used in the study of history (Wells II, 2012), monitoring of the natural environment (Guggenheim et al., 2006), or high-value scenes (e.g., cultural heritage) (Feng et al., 2015).

Early works focus on generating navigation information to assist users to adjust camera pose, such as the

computational rephotography method (Bae et al., 2010) and the homography-based active camera relocalization method (Feng et al., 2015). Through well designed fast matching strategy (including effective keyframe decision and feature substitution), Shi et al. (Shi et al., 2018) proposed a fast and reliable ACR approach that works well on mobile devices. Recently, Tian et al. (Feng et al., 2016; Tian et al., 2018) proposed a hand-eye calibration-free ACR strategy from a single 2D reference image, using a commercial robotic platform to automatically adjust the camera pose. Besides, they theoretically prove the convergence of their ACR strategy and achieve 0.1mm level camera relocalization precision in real-world applications. After that, Miao et al. (Miao et al., 2018) propose a depth camera based ACR strategy to further improve the robustness of ACR under textureless scenes. Despite the diversity and successes of previous ACR strategies, their convergence highly depends on the consistent lighting conditions, without which the foundation of relocalization convergence and accuracy is undermined.

2.2 Relative Camera Pose Estimation

Feature-based pose estimation. In the decades, relative camera pose estimation method based local feature, such as SIFT (Lowe, 2004), SURF (Bay et al., 2006), ORB (Rublee et al., 2011), have been proposed. Typical approaches based on feature matching includes 5-point solver (Nistér, 2004), 8-point solver (Hartley, 1997) etc. Although SIFT claims an advantage that it is robust to lighting changes when it first come out. Over the years of SLAM and SfM applications, SIFT do not performs satisfactorily for pose estimation under the highly variant illuminations.

Learning-based pose estimation. For a long time, researchers have been trying to learn the relative camera pose estimation by using neural networks. In the study of visual localization (Sarlin et al., 2019) and other tasks, some methods that directly regress the relative pose for two input images are proposed (Ummenhofer et al., 2017; Balntas et al., 2018; Laskar et al., 2017) to cooperate with image retrieval (Radenović et al., 2018) to achieve absolute pose estimation (Kendall et al., 2015). However, due to the complex conversion relationship from image space to $SE(3)$, the Learning-based method that directly learns the relative pose from images has been difficult to achieve good results.

Hybrid pose estimation. Another way to estimate relative pose is to train models for interest point detectors and descriptors fit for multiple-view feature matching (DeTone et al., 2018; Dusmanu et al., 2019; Yi et al., 2016). These hybrid methods, which only learns

image feature extraction and matching and leave the pose calculation to the epipolar constraint, show excellent performance in challenging image feature matching in specific dataset and provide reliable support for pose estimation in applications such as SLAM and SfM. However, the performance of these methods on unknown data will degrade, it do not achieve the same level of pose accuracy as Feature-based methods (Zhou et al., 2020; Sattler et al., 2019). Thus, these hybrid methods do not support the relative pose estimation accuracy requirement, e.g., an error less than 0.1° rotation, in ACR process, which is a high-level standard in applications as SLAM.

2.3 Fine-Grained Change Detection

Fine-grained change detection (FGCD) (Feng et al., 2015), designed to detect minute changes (pixel-level) between high-value scenes over long intervals. Unlike change detection problems (CD) that focus on object-level changes in the range of observations (Goyette et al., 2012; Maddalena and Petrosino, 2012), FGCD accomplish such tasks as fine-damage detection of precision instruments, minute-change detection of cultural relics, etc. The changes detected in these applications are often too subtle to be considered noise by CD.

Feng et al. first study the FGCD problem and present a feasible hybrid optimization scheme to separate the true fine-grained change map from the changes caused by varied imaging conditions (Feng et al., 2015). After that, Active camera relocalization (ACR) (Feng et al., 2016; Tian et al., 2018) makes FGCD simple and reliable by physically restoring the camera’s pose. However, in outdoor scenes, ACR is extremely unreliable due to completely uncontrollable lighting conditions, makes FGCD difficult or even fail.

3 Illumination-Invariant Active Camera Relocalization (i^2 ACR)

In this section, we propose a robust and fast ACR method to accurately align the observations under uncontrollable lighting conditions.

3.1 Preliminaries

Notation. In this paper, we use a 3D rotation $\mathbf{R} \in SO(3)$ and a 3D translation $\mathbf{t} \in \mathbb{R}^3$ to indicate the pose $\mathbf{P} \in SE(3)$ or the rigid body motion $\mathbf{M} \in SE(3)$. i.e., $\mathbf{P} = \begin{bmatrix} \mathbf{R} & \mathbf{t} \\ \mathbf{0}^T & 1 \end{bmatrix} \simeq \langle \mathbf{R}, \mathbf{t} \rangle$, the same to \mathbf{M} . Specifically,

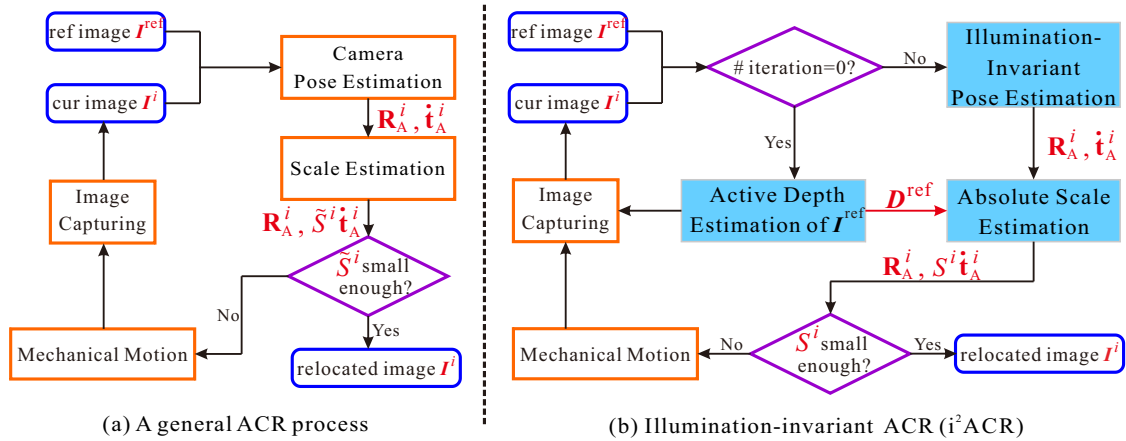


Fig. 2: Working flow of the Active Camera Relocalization (ACR) process. (a) and (b) show the framework of a general ACR process and the proposed Illumination-Invariant ACR (i^2 ACR), respectively.

\mathbf{t} denotes the direction of the translation. Additionally, considering the inevitable hand-eye relative pose $\mathbf{X} \in \text{SE}(3)$ ($\mathbf{X} \simeq \langle \mathbf{R}_X, \mathbf{t}_X \rangle$) in this problem, we use subscripts A and B to indicate the eye and the hand system, respectively. Specifically, $\mathbf{P}_A \simeq \langle \mathbf{R}_A, \mathbf{t}_A \rangle$ denotes the camera pose, whilst $\mathbf{P}_B \simeq \langle \mathbf{R}_B, \mathbf{t}_B \rangle$ represents the hand pose. Similarly, the rigid body motions \mathbf{M}_A and \mathbf{M}_B are named in the same way.

A general ACR process. Essentially, ACR seeks to identify optimal hand motion \mathbf{M}_B^* to relocate the camera from its initial pose \mathbf{P}_A^0 to the reference pose $\mathbf{P}_A^{\text{ref}}$,

$$\mathbf{M}_B^* = \arg \min_{\mathbf{M} \in \text{SE}(3)} \|\mathbf{X}\mathbf{M}\mathbf{X}^{-1}\mathbf{P}_A^0 - \mathbf{P}_A^{\text{ref}}\|_F^2, \quad (1)$$

where $\|\cdot\|_F$ is the Frobenius norm. It seems that all that is required is a reliable relative camera pose. However, it is expensive to frequently obtain the relative hand-eye pose in practice. Thus, the researchers (Tian et al., 2018) propose a general ACR process, as shown in Fig 2. They guess the \mathbf{X} by $\tilde{\mathbf{X}} = \mathbf{I}$ and execute a series of hand motions to achieve the equivalent effect of executing \mathbf{M}_B^* ,

$$\mathbf{M}_B^* = \prod_{i=n}^0 \tilde{\mathbf{M}}_B^n \tilde{\mathbf{M}}_B^{n-1} \cdots \tilde{\mathbf{M}}_B^i \cdots \tilde{\mathbf{M}}_B^0, \quad (2)$$

where $\tilde{\mathbf{M}}_B^i$ is the physically real state of the i -th guessed hand motion. We know $(\mathbf{P}_A^i)^{-1}\tilde{\mathbf{X}} = \tilde{\mathbf{X}}\tilde{\mathbf{M}}_B^i$, where $\mathbf{P}_A^i \simeq \langle \mathbf{R}_A^i, \mathbf{t}_A^i \rangle$ and $\tilde{\mathbf{M}}_B^i \simeq \langle \tilde{\mathbf{R}}_B^i, \tilde{\mathbf{t}}_B^i \rangle$. Thus, when $\tilde{\mathbf{X}} = \mathbf{I}$, $\tilde{\mathbf{M}}_B^i$ can be expressed as

$$\tilde{\mathbf{R}}_B^i = (\mathbf{R}_A^i)^{-1}, \quad \tilde{\mathbf{t}}_B^i = -(\mathbf{R}_A^i)^{-1}\mathbf{t}_A^i. \quad (3)$$

The authors of (Tian et al., 2018) prove that if the ACR process Eq. (2) iterates enough times, i.e., n becomes large enough, it will satisfactorily converge.

3.2 Overview

Compared with the general ACR process, our i^2 ACR process (see Fig 2) has improved in terms of both estimation and camera pose estimation. Based on a known physical robotic motion in an initialization module, we construct a linear system to obtain the absolute motion scale in each ACR iteration by minimizing the image warping error (*c.f.* Sec. 3.3). To estimate relative camera pose for each image pair requested, we extract the plane regions from the two images, respectively. We then use plane segments as an intermediate representation to facilitate feature matching, thus further boosting the pose estimation robustness under lighting changes, whilst maintaining a high degree of accuracy (*c.f.* Sec. 3.4).

3.3 Initialization for Absolute Scale Estimation

By using a reference image \mathbf{I}^{ref} taken in the past and a current image \mathbf{I}^i taken at this moment only, we can obtain the missing-scale relative camera pose, i.e., $\hat{\mathbf{P}}_A^i \simeq \langle \mathbf{R}_A^i, \mathbf{t}_A^i \rangle$. As set out in Fig. 3, we introduce an initialization module to acquire the absolute scale S^i for $\hat{\mathbf{P}}_A^i$ in each ACR iteration. In the following, we elaborate on the key steps for estimating S^i .

3.3.1 Ratio of absolute scale to depth

For simplicity, we assume the first camera pose is the world coordinate system. Subsequently, the relationship between the homogeneous coordinate point $\mathbf{q}^a \in \mathbb{R}^3$ on \mathbf{I}^a and the corresponding 3D point $\mathbf{Q}^a \in \mathbb{R}^3$ in world coordinate can be expressed as

$$\mathbf{Q}^a = \mathbf{K}^{-1}\mathbf{q}^a D^a, \quad (4)$$

where \mathbf{K} is the camera intrinsic matrix and D^a is the depth of \mathbf{q}^a . By taking $\mathbf{P}_A \simeq \langle \mathbf{R}_A, \mathbf{t}_A S \rangle$ as the camera relative pose between \mathbf{I}^a and a second image \mathbf{I}^b , we then get the 3D point $\mathbf{Q}^b \in \mathbb{R}^3$ in world coordinate by

$$\mathbf{Q}^b = \mathbf{R}_A^{-1} \mathbf{K}^{-1} \mathbf{q}^b D^b - \mathbf{R}_A^{-1} \mathbf{t}_A S, \quad (5)$$

where $\mathbf{q}^b \in \mathbb{R}^3$ is the homogeneous coordinate point on \mathbf{I}^b and D^b indicates the depth of \mathbf{q}^b . The matching homogeneous coordinate points between \mathbf{I}^a and \mathbf{I}^b correspond to the same 3D point \mathbf{Q} . Hence, minimizing the image warping error between \mathbf{I}^a and \mathbf{I}^b produces

$$\{\hat{D}_i^a, \hat{D}_i^b, \hat{S}\} = \arg \min_{D_i^a, D_i^b, S} \frac{1}{2} \sum_{i=1}^N \|\mathbf{Q}_i^a - \mathbf{Q}_i^b\|_F^2, \quad (6)$$

where $\|\cdot\|_F$ is the Frobenius norm and N is the number of matching feature points between \mathbf{I}^a and \mathbf{I}^b . By integrating Eqs. (4)–(6), the relationship between depth and absolute scale can be expressed as

$$\{\hat{D}_i^a, \hat{D}_i^b, \hat{S}\} = \arg \min_{D_i^a, D_i^b, S} \frac{1}{2} \sum_{i=1}^N F(D_i^a, D_i^b, S), \quad (7)$$

where the detailed expression of function $F(\cdot)$ is derived in the Appendix. Minimizing $F(\cdot)$ w.r.t. D_i^a , D_i^b and S resulting in a $3N \times (2N+1)$ homogeneous linear system, i.e., Eq. (25) in the Appendix, whose solution is

$$\mathbf{y} = [d_1^a, d_1^b, \dots, d_i^a, d_i^b, \dots, d_N^a, d_N^b, s], \quad (8)$$

Note, \mathbf{y} is the minimum non-zero solution of Eq. (25) and the lowercase d and s are not the depth and absolute scale values. The ratio between y_{2N+1} and y_i , ($i = 1, \dots, 2N$) represents the ratio between the absolute scale S and depth D , where y_i is the j -th element in \mathbf{y} .

3.3.2 Active depth estimation of \mathbf{I}^{ref}

At the very beginning of an ACR process, as shown in Fig 3, we first execute a known rigid body translation $\mathbf{M}_B^{\text{init}} \simeq \langle \mathbf{I}, \mathbf{t}_B^{\text{init}} \rangle$ and capture an intermediate image \mathbf{I}^{init} . Then we estimate the relative camera pose $\hat{\mathbf{P}}_A^{\text{init}} \simeq \langle \mathbf{I}, \mathbf{t}_A^{\text{init}} \rangle$ of \mathbf{I}^{init} and the current image \mathbf{I}^0 . Proceeding on this basis, the absolute scale S^{init} of $\hat{\mathbf{P}}_A^{\text{init}}$ can be calculated by $S^{\text{init}} = \|\mathbf{t}_B^{\text{init}}\| / \|\mathbf{t}_A^{\text{init}}\|$. In section 3.3.4, we show that the hand-eye relative pose \mathbf{X} does not affect the calculation of S^{init} , meaning that it does not affect the calculation of S^i in the subsequent ACR iterations.

Based on Eqs. (6)–(7), we construct a linear system from \mathbf{I}^0 and \mathbf{I}^{init} and then derive the solution

$$\mathbf{y}^{\text{init}} = [d_1^0, d_1^{\text{init}}, \dots, d_j^0, d_j^{\text{init}}, \dots, d_J^0, d_J^{\text{init}}, s^{\text{init}}], \quad (9)$$

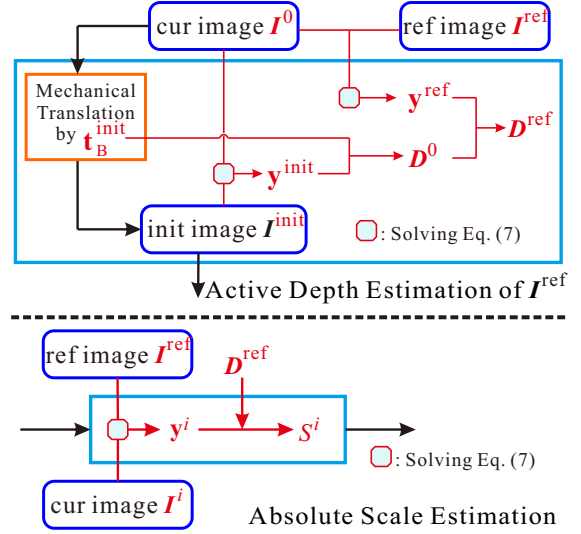


Fig. 3: Illustration of the Active Estimation of Depth and Absolute Scale Estimation modules of our i²ACR method (see Fig. 2).

where J is the number of the matching feature points between \mathbf{I}^0 and \mathbf{I}^{init} . As is apparent, we can get the sparse depth map \mathbf{D}^0 of the current image \mathbf{I}^0 through

$$\hat{D}_j^0 = d_j^0 \frac{S^{\text{init}}}{s^{\text{init}}}. \quad (10)$$

Similarly, for the reference image \mathbf{I}^{ref} and the current image \mathbf{I}^0 , we can obtain the relation

$$\mathbf{y}^{\text{ref}} = [d_1^{\text{ref}}, d_1^0, \dots, d_l^{\text{ref}}, d_l^0, \dots, d_L^{\text{ref}}, d_L^0, s^0], \quad (11)$$

where L is the number of the matching feature points between \mathbf{I}^{ref} and \mathbf{I}^0 , $L \leq J$. Hence, with the sparse depth map \mathbf{D}^0 and Eq. (11), we finally obtain a reference sparse depth map \mathbf{D}^{ref} through

$$\hat{D}_l^{\text{ref}} = \hat{D}_l^0 \frac{d_l^{\text{ref}}}{d_l^0}. \quad (12)$$

This depth map of \mathbf{I}^{ref} is the basis for the calculation of absolute scale in the subsequent ACR process.

3.3.3 Absolute scale estimation in each ACR iteration

The state-of-the-art ACR algorithm 5pt-ACR (Tian et al., 2018) guesses a scale \tilde{S}^i for \mathbf{t}_A^i through a bisection approaching strategy. Guessing a scale \tilde{S}^i for the i -th hand motion is indeed a reasonable solution, however, it usually takes a number of iterations to achieve ACR converge. As a result, a lot of time is spent on mechanical motion and image computation in practical applications. With our initialization module, the number of

ACR iterations can be greatly reduced by calculating rather than guessing the absolute scale.

For the reference image \mathbf{I}^{ref} and a current image \mathbf{I}^i in the i -th ACR iteration ($i \geq 1$), we have the relation

$$\mathbf{y}^i = [d_1^{\text{ref}}, d_1^i, \dots, d_p^{\text{ref}}, d_p^i, \dots, d_P^{\text{ref}}, d_P^i, s^i], \text{ s.t. } P \leq L, \quad (13)$$

where P is the number of the matching feature points between \mathbf{I}^i and \mathbf{I}^{ref} . With the sparse depth map \mathbf{D}^{ref} , we can calculate the absolute scale S^i by

$$S^i = \frac{1}{P} \left(\sum_{p=1}^P \frac{s^i \hat{D}_p^{\text{ref}}}{d_p^{\text{ref}}} \right). \quad (14)$$

Thus, we derive the relative camera pose $\mathbf{P}_A^i \simeq \langle \mathbf{R}_A^i, S^i \mathbf{t}_A^i \rangle$ and then execute the i -th hand motion \mathbf{M}_B^i according Eq. (3). Following multiple adjustments, ACR can be considered finished if S^i is small enough.

Although our strategy still requires multiple iterations to converge due to the unknown hand-eye relative pose \mathbf{X} , providing the exact absolute scale of the camera relative pose can expedite convergence considerably. Compared with 5pt-ACR, our approach can effectively reduce the iteration number of the ACR process from more than ten times to less than four times without compromising accuracy. See the experimental section for a detailed comparison and discussion of this point.

3.3.4 Analysis of the influence of hand-eye calibration

In this part, we will demonstrate that in the initialization module, even if we do not know the hand-eye relative pose \mathbf{X} , it will not affect the accuracy of S^{init} calculated by $S^{\text{init}} = \|\mathbf{t}_B^{\text{init}}\| / \|\mathbf{t}_A^{\text{init}}\|$. For convenience, we assume $\mathbf{P}_A^{\text{init}}$ is the relative pose between the current eye (camera) pose and initial eye (camera) pose while $\mathbf{P}_B^{\text{init}}$ is the relative pose between the current hand pose and initial hand pose.

By referring to the hand-eye relative pose \mathbf{X} , we can obtain the relations $\mathbf{X}\mathbf{M}_B^{\text{init}} = \mathbf{M}_A^{\text{init}}\mathbf{X} = (\mathbf{P}_A^{\text{init}})^{-1}\mathbf{X}$ (Tian et al., 2018). Hence, we have

$$\begin{aligned} \hat{\mathbf{M}}_B^{\text{init}} &= \arg \min_{\mathbf{M} \in \text{SE}(3)} \|\mathbf{X}\mathbf{M}\mathbf{X}^{-1}\mathbf{P}_A^{\text{init}} - \mathbf{I}\|_{\text{F}}^2 \\ &= \mathbf{X}^{-1}(\mathbf{P}_A^{\text{init}})^{-1}\mathbf{X}, \end{aligned} \quad (15)$$

where $\|\cdot\|_{\text{F}}$ is the Frobenius norm and \mathbf{I} is the unit matrix, $\mathbf{P}_A^{\text{init}} \simeq \langle \mathbf{I}, \mathbf{t}_A^{\text{init}} \rangle$. We split Eq. (15) into its rotation and translation parts, which yields

$$\mathbf{I} = (\mathbf{R}_X)^{-1}\mathbf{I}\mathbf{R}_X, \quad (16)$$

$$\begin{aligned} \mathbf{t}_B^{\text{init}} &= (\mathbf{R}_X)^{-1}\mathbf{I}\mathbf{t}_X - (\mathbf{R}_X)^{-1}\mathbf{I}\mathbf{t}_A^{\text{init}} - (\mathbf{R}_X)^{-1}\mathbf{t}_X \\ &= -(\mathbf{R}_X)^{-1}\mathbf{t}_A^{\text{init}}. \end{aligned} \quad (17)$$

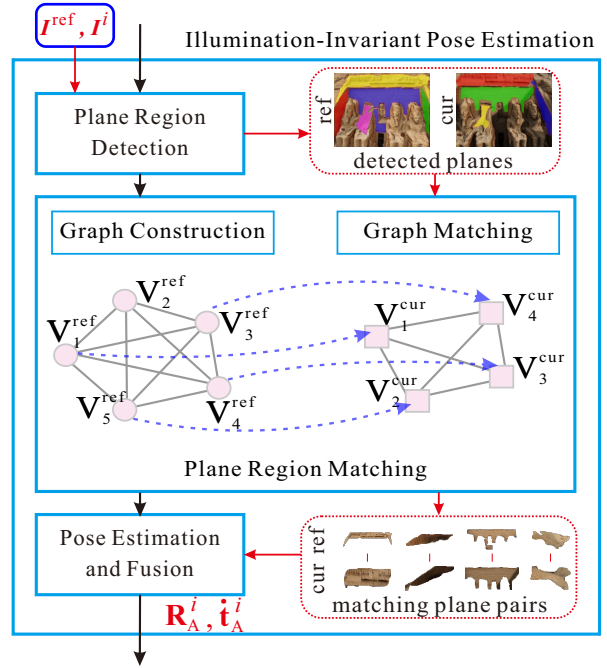


Fig. 4: Illustration of the Illumination-Invariant Pose Estimation (i²PE) module in Fig. 2.

According to Eq. (17), it can reasonably be concluded that absolute scale S^{init} can be calculated by $\|\mathbf{t}_B^{\text{init}}\| = \|\mathbf{t}_A^{\text{init}}\| = S^{\text{init}}\|\mathbf{t}_A^{\text{init}}\|$ without first knowing the hand-eye relative pose. More specifically, by executing a known rigid body translation, we can accurately estimate the absolute scale S^i in the subsequent ACR iterations without knowing the hand-eye relative pose.

3.4 Illumination-Invariant Pose Estimation

For the two images \mathbf{I}^{ref} and \mathbf{I}^{cur} taken under different lighting conditions, as shown in Fig. 4, we use planes as intermediate representations to effectively improve the robustness and reliability of pose estimation. As has been shown, image features such as SIFT reflect the local gradient distribution of the image. For the planar region in the image, lighting changes will change the pixel value, although they will have a limited influence on the gradient distribution. Due to this, the planar structure and the matching between plane regions can eliminate the adverse effects of large illumination variances (see experimental results for the verification). In this subsection, we introduce the proposed illumination-invariant pose estimation (i²PE) and describe in detail how to use planes as intermediate representations to boost pose estimation robustness under different illuminations.

3.4.1 Plane region detection

We apply Plane R-CNN (Liu et al., 2019) to extract the plane regions from \mathbf{I}^{ref} and \mathbf{I}^{cur} , respectively. Plane R-CNN employs a variant of Mask R-CNN (He et al., 2017) to detect planes and performs best in the plane detection task. However, there are still inevitable errors near the plane boundary of the detection results. Since the feature descriptors near the plane boundaries are subjected to lighting changes. In such conditions, improving the segmentation accuracy on plane boundaries does not make much sense. Therefore, we subjected the detected planes to mild morphological erosion (Jackway and Deriche, 1996) to further improve pose estimation accuracy.

3.4.2 Plane region matching

Let $\mathcal{I}^{\text{ref}} = \{\mathbf{P}_h^{\text{ref}}\}_{h=1}^H$ be the collection of H planes detected from \mathbf{I}^{ref} , with $\mathbf{P}_h^{\text{ref}}$ being the h -th detected plane. Similarly, let $\mathcal{I}^{\text{cur}} = \{\mathbf{P}_m^{\text{cur}}\}_{m=1}^M$ be the collection of M planes detected in \mathbf{I}^{cur} . To find the matching relations implied in \mathcal{I}^{ref} and \mathcal{I}^{cur} , i.e., the same plane region captured by the two images, we model it as a graph matching problem. As shown in Fig. 4, for \mathcal{I}^{ref} , the node-set \mathcal{V}^{ref} of the undirected graph $\mathcal{G}^{\text{ref}} = \{\mathcal{V}^{\text{ref}}, \mathcal{E}^{\text{ref}}\}$ denotes the H detected planes. The undirected edge-set \mathcal{E}^{ref} indicates the minimum Euclidean distance between any two detected planes in \mathcal{I}^{ref} . We construct undirected graph \mathcal{G}^{cur} from \mathcal{I}^{cur} in the same way. Then, matching the two graphs \mathcal{G}^{ref} and \mathcal{G}^{cur} is to identify an optimal node-to-node correspondence $\mathbf{U} \in \{1, 0\}^{H \times M}$, where $\mathbf{U}_{ac} = 1$ when the nodes $V_a^{\text{ref}} \in \mathcal{V}^{\text{ref}}$ and $V_c^{\text{cur}} \in \mathcal{V}^{\text{cur}}$ are matched, $\mathbf{U}_{ac} = 0$ for otherwise. In this paper, the assignment matrix \mathbf{U} has the following condition,

$$\mathcal{U} = \left\{ \mathbf{U} \mid \mathbf{U} \in \{1, 0\}^{H \times M}, \mathbf{U}^T \mathbf{1}_H \leq \mathbf{1}_M, \mathbf{U} \mathbf{1}_M = \mathbf{1}_H \right\}, \quad (18)$$

where $\mathbf{1}_M$ and $\mathbf{1}_H$ are unit vectors with dimension M and H , respectively. Eq. (18) constrains the plane matching problem to be a one-to-one mapping model. Considering \mathcal{G}^{ref} and \mathcal{G}^{cur} may have the different sizes, we use the inequality in Eq. (18) to indicate the assumption that $H \leq M$.

The matching problem can be solved by maximizing an objective function that measures the node and edge affinities between \mathcal{G}^{ref} and \mathcal{G}^{cur} . As such, we use the potential $w_v(V_a^{\text{ref}}, V_c^{\text{cur}})$ to measure the similarity between nodes V_a^{ref} and V_c^{cur} . Additionally, we use the potential $w_e(E_{ab}^{\text{ref}}, E_{cd}^{\text{cur}})$ to measure the similarity between edges E_{ab}^{ref} and E_{cd}^{cur} . Specifically, $w_v(V_a^{\text{ref}}, V_c^{\text{cur}})$ is measured by the number of matching feature points between $\mathbf{P}_a^{\text{ref}}$ and $\mathbf{P}_c^{\text{cur}}$, $w_e(E_{ab}^{\text{ref}}, E_{cd}^{\text{cur}})$ is measured by

the difference between the minimum Euclidean distance of $\mathbf{P}_a^{\text{ref}}$ to $\mathbf{P}_b^{\text{ref}}$ and $\mathbf{P}_c^{\text{cur}}$ to $\mathbf{P}_d^{\text{cur}}$.

We integrate these two types of similarities through an affinity matrix $\mathbf{W} \in \mathbb{R}^{MH \times MH}$, in which the diagonal element corresponds to the unary potential $w_v(V_a^{\text{ref}}, V_c^{\text{cur}})$ and the non-diagonal element corresponds to the pairwise potential $w_e(E_{ab}^{\text{ref}}, E_{cd}^{\text{cur}})$. Based on the description above, we generate the objective function

$$\mathbf{U}_c^T \mathbf{W} \mathbf{U}_c = \sum_{U_{ac}=1} w_v(V_a^{\text{ref}}, V_c^{\text{cur}}) + \sum_{\substack{U_{ac}=1 \\ U_{bd}=1}} w_e(E_{ab}^{\text{ref}}, E_{cd}^{\text{cur}}), \quad (19)$$

where \mathbf{U}_c is the column expansion of \mathbf{U} . Then, the plane region matching problem can be addressed by identifying the optimal assignment matrix \mathbf{U}^*

$$\mathbf{U}^* = \arg \max_{\mathbf{U}} \mathbf{U}_c^T \mathbf{W} \mathbf{U}_c, \quad \text{s.t. } \mathbf{U} \in \mathcal{U}. \quad (20)$$

We use the deformable graph matching method (Zhou and De la Torre, 2013) to solve Eq. (20) and then obtain the K matching plane region pairs $\mathcal{M} = \{(\mathbf{P}_i^{\text{ref}}, \mathbf{P}_i^{\text{cur}})\}_{i=1}^K$ from the optimal assignment matrix \mathbf{U}^* .

3.4.3 Pose estimation and fusion

Given a matching plane pair $(\mathbf{P}_i^{\text{ref}}, \mathbf{P}_i^{\text{cur}})$, the camera relative pose can be estimated by decomposing the homography matrix calculated from $\mathbf{P}_i^{\text{ref}}$ and $\mathbf{P}_i^{\text{cur}}$. Compared to the other feature-based pose estimation algorithms, e.g., 5-point solver (Nistér, 2004), which is essentially unaffected by the planar degeneracy and works, the decomposing homography matrix (Faugeras and Lustman, 1988) offers obvious advantages in relation to noise interference (see experimental results for the verification).

In theory, the K relative poses estimated from the K matching plane pairs in \mathcal{M} are the same. We fuse those that exhibit variance according to their reliability to further ensure accuracy and robustness. In this regard, reliability can be considered from two aspects: 1) *Number*, we prefer the estimated pose from the plane pair which has numerous matching feature points. 2) *Distribution*, we prefer the estimated pose from the plane pair which has a more uniform distribution of feature points.

By using planes as an intermediate representation, we obtain reliable and accurate pose estimation results under highly variant illuminations. In addition, the matching between the planes does not consider those variation areas, such that, our method can also effectively eliminate the interference of the partial region changes on camera pose estimation.

Table 1: Time performance and AFD values for 8 scenes. The red values represent failed relocalizations. See text for details.

Scene	5pt-ACR			i ² ACR		
	AFD	Iteration times	Time (s)	AFD	Iteration times	Time (s)
constantL1	0.809	13.4	254.6	0.821	3.4	100.6
constantL2	1.077	13.8	266.8	1.002	3.2	104.8
constantL3	0.519	13.2	259.6	0.486	3.0	105.2
constantL4	0.765	13.6	261.2	0.793	2.8	101.8
constantL_average	0.793	13.5	260.6	0.776	3.1	103.1
variedL1	143.513	16.6	298.4	0.972	2.8	97.8
variedL2	76.749	17.4	321.6	1.003	3.8	103.8
variedL3	161.333	16.2	289.2	0.690	3.0	100.6
variedL4	96.401	17.8	323.4	0.851	3.2	104.2
variedL_average	119.499	17.0	308.2	0.879	3.2	101.6

4 Experimental Results

4.1 Setup

In the ACR verification experiments, we compare the proposed illumination-invariant active camera relocalization (i²ACR) with the state-of-the-art ACR strategy (5pt-ACR) (Tian et al., 2018). We build 8 different scenes to execute the ACR process on the monitoring platform with a Canon 5D MarkIII camera. These scenes can be divided into 4 scenes with varied lighting conditions (variedL1–4), and 4 normal scenes with constant lighting conditions (constantL1–4). We use the average feature-point displacement (AFD) Tian et al. (2018) to quantitatively measure the relocalization accuracy,

$$\text{AFD}(\mathbf{f}_{\text{ref}} - \mathbf{f}_{\text{cur}}) = \frac{1}{l} \sum_{i=1}^l \|\mathbf{f}_{\text{ref}}^i - \mathbf{f}_{\text{cur}}^i\|_2, \quad (21)$$

where \mathbf{f}_{ref} and \mathbf{f}_{cur} are the matching feature-point coordinates in the reference image and the current relocalized image, respectively. Meanwhile, l is the number of matches. In the following, we will set out a detailed explanation and analysis of each experiment.

4.2 Comparison of i²ACR with the state-of-the-art

For 5pt-ACR and our i²ACR algorithm, we perform ACR for each algorithm five times for each of the 8 scenes, i.e., constantL1–4 and variedL1–4. To guarantee fairness, we also reproduce the reference and initial camera poses for each independent test of the same

scene. Fig. 5 gives the visual results of the ACR two groups in constantL1 (the first two rows) and variedL1 (the last two rows). Detailed time performance and average AFD values are listed in Table 1.

4.2.1 Robustness analysis

Table 1 shows that the accuracy of our method is comparable to the 5pt-ACR’s in constantL1–4, which is reasonable. As shown in the first two rows of Fig. 5, compared to 5pt-ACR, i²ACR only reduces the number of feature matches involved in pose estimation. Moreover, there are almost no mismatched feature matches after RANSAC (Fischler and Bolles, 1981) when the lighting conditions do not change. From this, it can be concluded that the pose estimation accuracy of both 5pt-ACR and ours can satisfactorily support the ACR process.

Compared to the 5pt-ACR strategy used in variedL1–4, ours demonstrated greater superiority. By using the 5pt-ACR strategy, the ACR process failed in all experiments under variedL1–4. As shown in the third row of Fig. 5, sharp differences in lighting change the appearance of scenes (especially scenes featuring 3D structure), hence the feature point descriptors involved in pose estimation change, which give rise to the dramatic mismatching of feature points even after RANSAC. Thus, the accuracy performance of 5pt-ACR degrades significantly when the two observations have highly varied illuminations. In contrast, i²ACR shows the same accuracy performance in variedL1–4 as in constantL1–4. The fourth row of Fig. 5 visualizes an example of feature matching in the first iteration of i²ACR executed

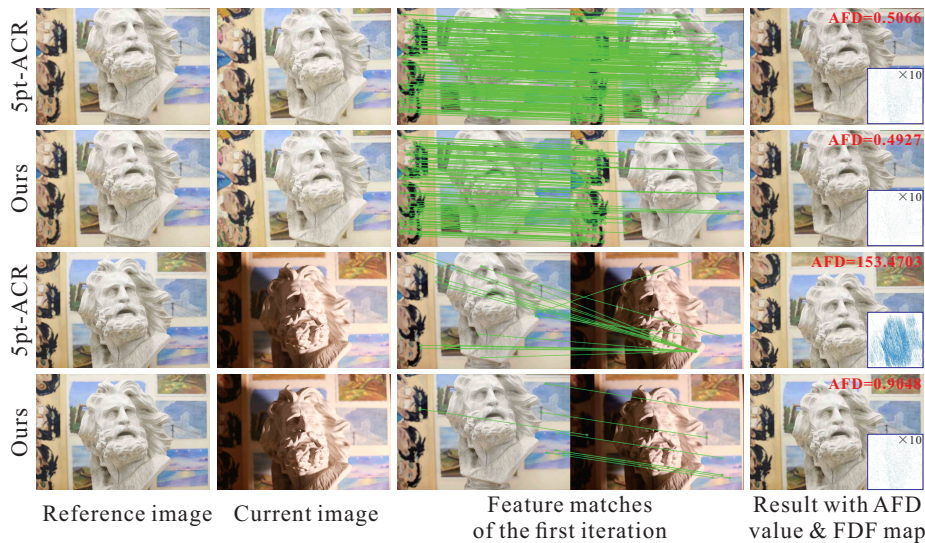


Fig. 5: Two groups of ACR with (the third and fourth rows) and without (the first and second rows) lighting difference, respectively. In the third column, we visualize the feature matches at the first iteration of each ACR process. We restore the lighting conditions to the same as the reference when ACR is finished, then we calculate the AFD values of each ACR process, and the results are shown in the fourth column.

in variedL1. As can be seen from Fig. 5 and Table 1, since planes are used as an intermediate representation to qualify the search space for feature matching, i^2 ACR exhibits a significant advantage in accuracy and robustness, thus, effectively supporting the valid ACR process.

4.2.2 Convergence rate analysis

We analyze all of the ACR experiments and average the results in constantL1-4 and variedL1-4, respectively. As shown in Fig. 6, the variation trend of relocalization error (rotation difference and translation error) shows the ACR convergence process. Specifically, we use Euler angles in three axes to denote the rotation of relative pose for convenience. When considering only the performance of effective ACR processes (experiments under constantL1-4), Fig. 6(b) demonstrates that i^2 ACR converges 3.5 times faster than the state-of-the-art 5pt-ACR, Table 1 shows that the real application time will be reduced by 60% compared with the state-of-the-art 5pt-ACR. This reduction is largely due to our method provides the absolute scale for each \mathbf{M}_B^i , thus expediting the convergence of Eq. (2). By way of contrast, 5pt-ACR relies on guessing the translation scale, which requires more adjustments to converge.

Note, because of the unknown relative hand-eye \mathbf{X} , which we treat it as identity matrix \mathbf{I} , and the imperfect pose estimation, ACR cannot guarantee camera pose convergence in just one step. As such, it takes several iterations to eliminate the influence of \mathbf{X} and imperfect pose estimation results and ensure that ACR converges,

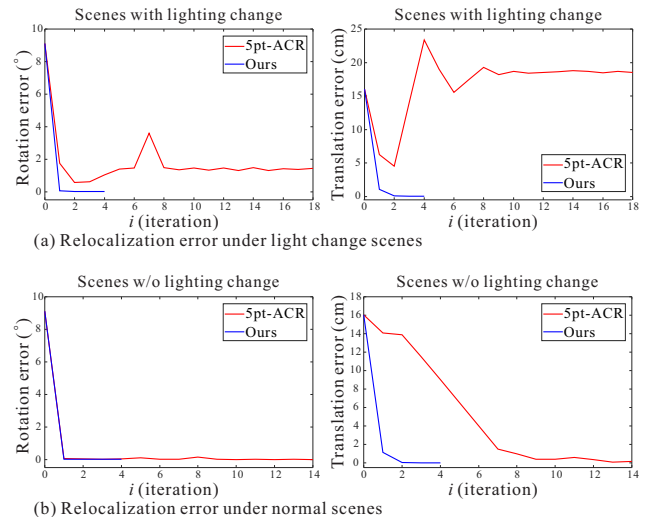


Fig. 6: Average convergence process of \mathbf{R}_A and \mathbf{t}_A in constantL1-4 and variedL1-4. (a) shows the convergence curves under scenes with lighting change while (b) shows the convergence curves under scenes without lighting change.

see (Tian et al., 2018) for details. However, as can be seen from Table 1, the iteration number (average 3.15 times) of i^2 ACR is much less than the iteration number of 5pt-ACR (average 15.25 times).

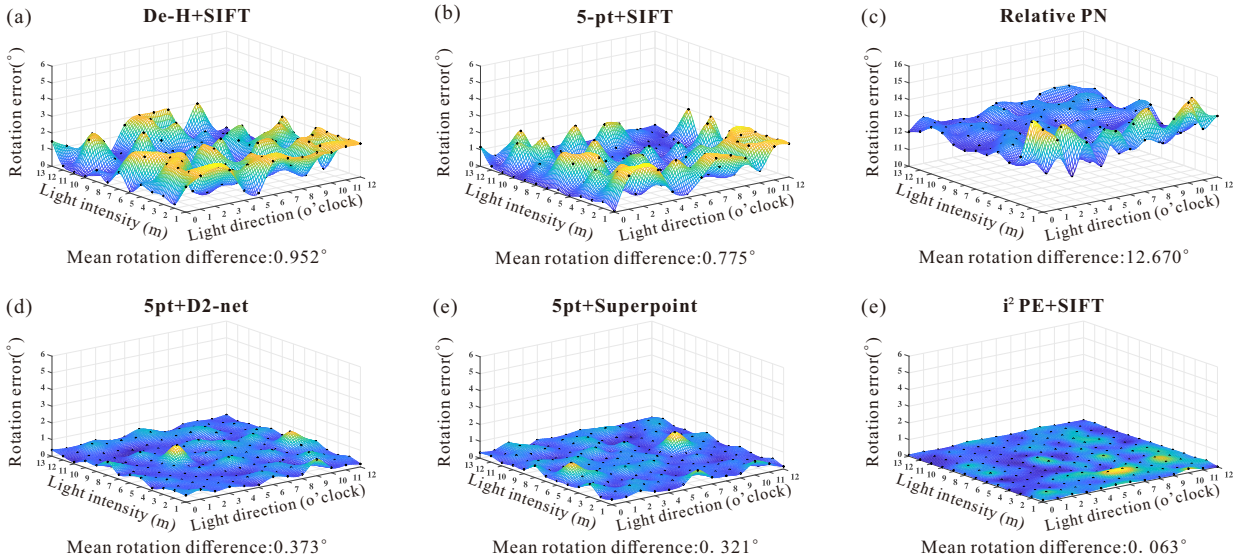


Fig. 7: (a)–(f) shows the representative comparison results of our pose estimation method and baselines under varied lighting intensities and directions, the smoother the heat-map, the more robust the method. Note that our method performs superior to baselines for accuracy and robustness.

4.3 Analysis of Relative Pose Estimation

As noted above, the ACR relocalization precision relies on the accuracy of relative camera pose estimation. In this subsection, we further explore and verify the effectiveness of i^2 ACR by comparing the relative pose estimation performance of the proposed pose estimation method in i^2 ACR with that of other pose estimation method in situations with varying lighting.

4.3.1 Datasets and baselines

Datasets. To evaluate the proposed i^2 PE on challenging data exhibiting a large illumination difference, we use Unity 3D to create a virtual environment and quantitatively control the changes in lighting intensity and direction. Specifically, we design 13 varied lighting directions, i.e., 1, ..., 12 o'clock side lightings and front lighting. We also design 13 different lighting intensities; the change in lighting intensity is equivalently achieved by controlling the distance between the light source and the scene. For convenience, we represent lighting intensity in terms of distance in this paper. In particular, we treat the front lighting direction with the intensity of 7 meters as the standard environment.

In this lighting-controlled virtual environment, we construct a dataset consisting of 510 images of three building models (170×3). For each building, we capture a reference image in the standard environment and then control the virtual camera to execute a certain motion \mathbf{M}_A . By adjusting the lighting direction (1, ..., 12

o'clock directions and the front direction) and intensity (1, 2, ..., 13 m), we take 169 current images under each intensity and each direction condition. Ultimately, we generate 507 reference-current image pairs from the dataset.

Metrics and baselines. In this paper, we employ the angular error ($^\circ$) to measure the correction of the estimated rotation. For the estimated translation, we use the angular error ($^\circ$) to measure the correction of its direction. Our baselines for comparison are as follows, ranging from purely hand-crafted to purely data-driven models. **Feature-based:** (1) *De-H* (Faugeras and Lustman, 1988) + *SIFT*, (2) *5-point solver* (Nistér, 2004) + *SIFT*. **Learning-based:** (3) *Relative PN* (Laskar et al., 2017). **Hybrid:** (4) *De-H* + *D2-net* (Dusmanu et al., 2019), (5) *5-point solver* + *D2-net*, (6) *De-H* + *Superpoint* (DeTone et al., 2018), (7) *5-point solver* + *Superpoint*. For convenience, we call 5-point solver 5-pt in the rest of this paper.

Among them, *De-H* estimates the relative pose by decomposing the homography matrix. In our experiments, we use the implementation of it in ORB-SLAM (Mur-Artal and Tardós, 2017), a little bit different is that we use *SIFT* instead of ORB for feature extraction and description. *Relative PN* is a learning-based approach for camera relocalization. When given a query image, it first retrieves similar database images and then predicts the relative pose between the query and the database images. In our experiments, we treat the reference image as the database image whilst the current image is the query. We specify the reference image (database)

Table 2: Comparisons of i^2PE and baselines. We also test the performance of using Superpoint and D2-net instead of SIFT in i^2PE , respectively

method		w/o lighting difference		with lighting difference	
		\mathbf{R} error($^\circ$)	$\mathbf{\hat{t}}$ error($^\circ$)	\mathbf{R} error($^\circ$)	$\mathbf{\hat{t}}$ error($^\circ$)
Feature-based	De-H+SIFT	0.269	2.377	0.952	4.006
	5-pt+SIFT	0.004	0.082	0.775	5.532
Hybrid	De-H+Superpoint	0.920	0.778	1.138	0.721
	5-pt+Superpoint	0.308	0.108	0.321	0.155
	De-H+D2-net	1.208	1.991	2.032	1.837
	5-pt+D2-net	0.300	0.801	0.373	2.159
Learning-based	Relative PN	12.371	11.744	12.670	11.623
Ours	i^2PE +Superpoint	0.311	0.108	0.323	0.155
	i^2PE +D2-net	0.351	0.922	0.357	1.966
	i^2PE +SIFT	0.004	0.089	0.063	0.097

corresponding to the current image (query) rather than retrieving it. D2-Net and Superpoint are learning-based method that learns the description and detection of local features. In our experiments, we apply them to replace the SIFT-based feature extraction and description used in De-H+SIFT and 5-pt+SIFT for pose estimation, respectively.

4.3.2 Less learn is more

Comparison results. Table 2 compares the accuracy of our approaches to the baselines. As can be seen, when there are lighting differences between the reference and current images, i^2PE +SIFT performs superior to the others. When there is no lighting difference, our method performs almost as well as 5-pt+SIFT, while performing best. Fig. 7 compares the robustness of our approaches to the baselines by using the rotation error of the poses estimated under varied lighting conditions. The result shows that our proposed pose estimation method i^2PE +SIFT performs best. The mean rotation difference is only 0.063° and the change in rotation error is almost irrelevant to the illumination variation. Referring to Table 2 and Fig. 7, with regard to relative camera pose estimation, the Learning-based method and the hybrid method are not particularly sensitive to the illumination changes. Moreover, when there are illumination differences between the reference and current images, the hybrid method even performs better than the Feature-based method. Unfortunately, although this precision may satisfy application requirements such as visual localization, it is far from sufficient for FGCD tasks.

What should neural networks learn? For a long time, researchers have been trying to learn the relative camera pose estimation by using neural networks. However, due to the complex conversion relationship from image space to $SE(3)$, it is difficult to generate satisfactory results using the Learning-based method that directly learns the relative pose from images. Although the hybrid method, which only learns image feature extraction and matching and leaves the calculation to the epipolar constraint, yields better results than the Learning-based method, it do not achieve the same level of pose accuracy as Feature-based methods (Zhou et al., 2020; Sattler et al., 2019).

The overarching advantage of deep learning lies in image understanding tasks such as classification and segmentation. As has been shown, image features like SIFT reflect the local gradient distribution of the image. For the planar region in the image, lighting changes will change the pixel value, although they have a limited influence on the gradient distribution. As shown in Fig. 8, SIFT feature descriptors located in the plane region are less impacted by lighting changes. Specifically, the Euclidean distance of SIFT feature descriptors which we called sift map in Fig. 8 denotes the difference between SIFT feature descriptors at the same location in the reference and current images, wherein the brighter the pixel, the bigger the corresponding descriptor difference. Thus, we use neural networks to segment the planar region to help pose estimation. In addition, as an intermediate representation in feature matching, effective plane matching further limits the retrieval range in the process of feature-point matching, thus greatly reducing the occurrence of feature-point mismatching.

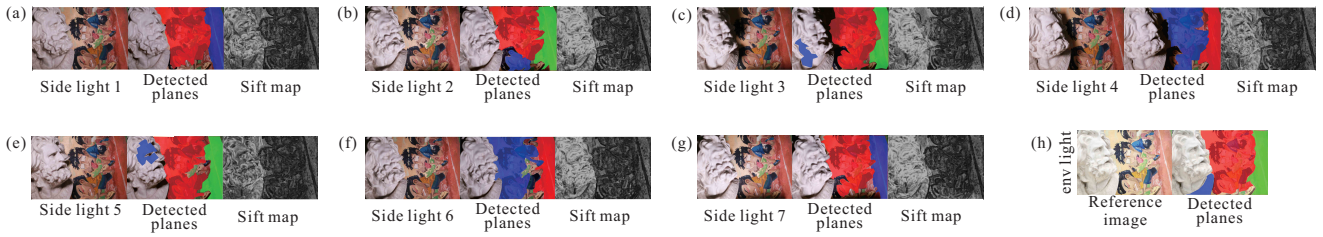


Fig. 8: (a)–(g) show the visual results of plane detection and Euclidean distance maps of SIFT feature descriptors between environment lighting image (h) and varied side lightings. Note that the red, blue and green area are the plane detection results.

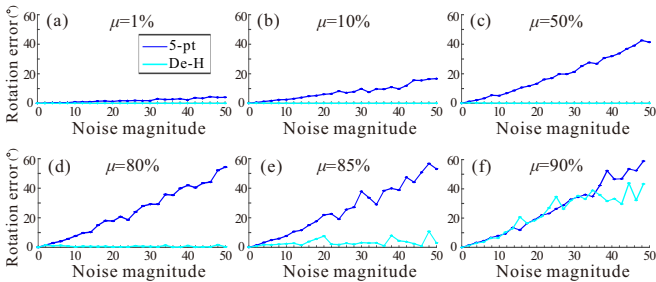


Fig. 9: Relation of noise magnitude on matching points and the angle (axis-angle) error, under varied noise ratios.

Strictly speaking, our method should also be viewed as a hybrid method. One of the main reasons why it can achieve better results than D2-Net+5-pt is that the data-driven method experiences generalization problems, as shown in Fig. 8. Moreover, Plane R-CNN has difficulties guaranteeing the accuracy of the segmentation results on the plane boundary. Therefore, in the subsequent feature extraction and matching, we abandon the boundary area of the plane segments, thus avoiding the disadvantages flowing from network model generalization to a considerable extent.

4.3.3 Why not use the 5-point solver

5pt-ACR uses the *SIFT + 5-point solver* for pose estimation and performs well when applied to pure planar scenes, such as ancient murals. Our *i*²ACR selects *SIFT + De-H* for pose estimation and also performs well. We then design a simulation experiment to verify the camera pose estimated by decomposing the homography matrix from a single plane that is more stable than that estimated by the 5-point solver.

The experimental data are 1000 virtual space points in a plane. To simulate the real scene and the real camera as best we could, we set up a virtual camera with the same parameters as Canon 5D MarkIII. We project space points onto the virtual camera imaging

plane and obtain the corresponding reference 2-D coordinates. Next, we control the virtual camera to execute a rigid body motion and obtain the current 2-D coordinates of those space points. After that, we add noises ($\mu \times 1000$, $0 \leq \mu \leq 100\%$) of different magnitude r which uniformly increases from 0 to 50 with a step size of 2. Finally, we estimate the motion of the virtual camera by 5-pt and De-H, respectively. Note that the noises added in this experiment come from a uniform distribution $U(-r, r)$.

Fig. 9 shows 6 results of this experiment. We represent the ground truth and the estimated rotation in terms of the axial angle representation. Since the calculated translation only indicates the direction and does not contain the absolute scale, we only compare the calculated rotation with the ground truth. The experimental results show that even though the noise magnitude is slight (e.g., 1%), the angle estimated by 5-pt is still worse. Meanwhile, when $\mu < 80\%$, De-H is strongly robust to feature matching noises. As for $\mu \geq 90\%$, both the angle estimated by De-H and 5-pt are unreliable. Note that the severe matching errors that invalidate the two methods are reasonable. Hence, in *i*²ACR, we use SIFT+De-H for pose estimation.

4.4 Real-world applications

As aforementioned, ACR study is originally motivated by long-time-interval fine-grained change monitoring and measurement of cultural heritages in wild hosting environments. This is a very important and challenging problem that is an essential part for preventive conservation of cultural heritages (Tian et al., 2018). This is a very important and challenging problem that is an essential part for preventive conservation of cultural heritages (Staniforth, 2013).

In the last three years, using the proposed *i*²ACR approach, we have conducted monthly fine-grained status inspection of several world cultural heritages in China, including the Palace Museum (PM), the Summer Palace

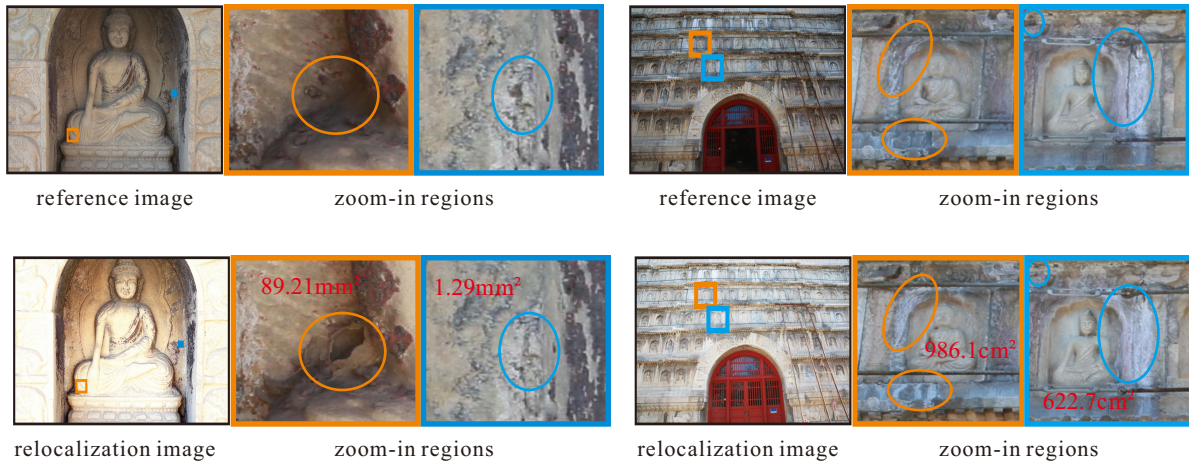


Fig. 10: Real-world fine-grained change monitoring cases in the Five-Pagoda Temple. The reference image is captured in June 2019, the relocalized image is captured in August 2019.

Table 3: Time performance and AFD error in real-world applications. Note that the PM, the SP, the FPT are the Palace Museum, the Summer Palace, and the Five-Pagoda Temple, respectively.

Scene	5pt-ACR		i ² ACR	
	AFD	Time (s)	AFD	Time (s)
PM	0.901	271.250	0.973	106.375
SP	2.710	262.125	1.963	102.750
FPT	failed	failed	2.005	105.125

(SP), Dunhuang Mogao Grottoes, Humble Administrator’s Garden, and the Five-Pagoda Temple (FPT), covering indoor ancient murals and outdoor ancient buildings, earthen sites stone-sculpted relics.

Table 3 shows the average AFD scores for each piece of historical heritage by using 5pt-ACR and our i²ACR strategy, respectively. There are 8 scenes for each historical heritage. The results in Table 3 further illustrate the effectiveness and superiority of i²ACR. Note that the monitoring task of the Palace Museum is carried out in a controlled indoor lighting condition, and the outdoor lighting environment of the Summer Palace is essentially the same as when the reference images were taken. Fig. 10 gives some examples of real fine-grained deterioration changes of the Five-Pagoda Temple, discovered by our i²ACR strategy from June to August 2019. We also try to use 5pt-ACR to relocate the camera pose to the reference but failed due to the varied illumination difference compared with the reference. Intuitively, we adjusted the zoom-in regions of the reference and relocalization image in Fig. 10 to make their respective illuminations consistent.

Table 3 and Fig. 10 fully demonstrate that our proposed method makes up for the lack of outdoor fine-grained change monitoring tasks. This is important as many high-value targets require us to grasp their periodic fine-grained changes.

5 Conclusion

In this paper, we have addressed illumination robustness and convergence speed, two critical issues of active camera relocalization (ACR), by proposing i²ACR, a new fast and robust ACR scheme. Specifically, we first design an initialization module, thus, construct a linear system to obtain the absolute motion scale in each ACR iteration by minimizing the image warping error. Second, we use plane segments as an intermediate representation to facilitate feature matching, thus further boosting pose estimation robustness and reliability under lighting variances. Since the improvement both in relative pose estimation and scale estimation, our i²ACR achieves 1.6× faster convergence speed, much better relocalization accuracy and robustness over state-of-the-art ACR competitors, especially in the wild.

Furthermore, we discuss how to balance the deep learning and the traditional methods in a relative pose estimation pipeline under the premise of pursuing high precision results. As verified by our experiment, image features like SIFT on the planar structures are less subjected to the lighting change. Thus, we use neural networks to segment the planar region to help pose estimation. Compared with the feature-based, learning-based, and hybrid pose estimation methods, ours shows great superiority in both accuracy and generalization.

A Detailed derivation

In this appendix, we show the detailed steps to get the ratio between the depth and the absolute scale from the Eq. (4)–(7). First, we specify the following mathematical representations:

$$\begin{aligned}
\alpha &= \mathbf{q}^{a\top} (\mathbf{K}^{-1})^\top \mathbf{K}^{-1} \mathbf{q}^a, \\
\beta &= \mathbf{q}^{a\top} (\mathbf{K}^{-1})^\top \mathbf{R}^{-1} \mathbf{K}^{-1} \mathbf{q}^b, \\
\gamma &= \mathbf{q}^{a\top} (\mathbf{K}^{-1})^\top \mathbf{R}^{-1} \dot{\mathbf{t}}_A, \\
\delta &= \mathbf{q}^{b\top} (\mathbf{K}^{-1})^\top (\mathbf{R}^{-1})^\top \mathbf{R}^{-1} \mathbf{K}^{-1} \mathbf{q}^b, \\
\epsilon &= \mathbf{q}^{b\top} (\mathbf{K}^{-1})^\top (\mathbf{R}^{-1})^\top \mathbf{R}^{-1} \dot{\mathbf{t}}_A, \\
\zeta &= (\dot{\mathbf{t}}_A)^\top (\mathbf{R}^{-1})^\top \mathbf{R}^{-1} \dot{\mathbf{t}}_A.
\end{aligned} \tag{22}$$

For the item in Eq. (6), we have the equivalent expression:

$$\|\mathbf{Q}_i^a - \mathbf{Q}_i^b\|_2^2 = (\mathbf{Q}_i^a - \mathbf{Q}_i^b)^\top (\mathbf{Q}_i^a - \mathbf{Q}_i^b). \tag{23}$$

Integrating Eqs. (4), (5) and (22)–(23), we can obtain the detailed expression of $F(\cdot)$ in Eq. (7):

$$\begin{aligned}
\frac{1}{2} \|\mathbf{Q}_i^a - \mathbf{Q}_i^b\|_2^2 &= \frac{1}{2} \alpha_i (D_i^a)^2 - \beta_i (D_i^a D_i^b) + \gamma_i (D_i^a S) \\
&\quad + \frac{1}{2} \delta_i (D_i^b)^2 - \epsilon_i (D_i^b S) + \frac{1}{2} \zeta_i S^2 \\
&= F(D_i^a, D_i^b, S),
\end{aligned} \tag{24}$$

obviously, F is a convex function. For the objective function Eq. (7), by computing the derivative of the F with respect to the D_i^a , D_i^b , S and setting to zero, we have a $3N \times (2N + 1)$ linear system:

$$\begin{pmatrix}
\alpha_1 & -\beta_1 & 0 & 0 & \cdots & \gamma_1 \\
-\beta_1 & \delta_1 & 0 & 0 & \cdots & -\epsilon_1 \\
\gamma_1 & -\epsilon_1 & 0 & 0 & \cdots & \zeta_1 \\
0 & 0 & \alpha_2 & -\beta_2 & \cdots & \gamma_2 \\
0 & 0 & -\beta_2 & \delta_2 & \cdots & -\epsilon_2 \\
0 & 0 & \gamma_2 & -\epsilon_2 & \cdots & \zeta_2 \\
\vdots & \vdots & & \ddots & & \vdots \\
0 & \cdots & \cdots & \alpha_N & -\beta_N & \gamma_N \\
0 & \cdots & \cdots & -\beta_N & \delta_N & -\epsilon_N \\
0 & \cdots & \cdots & \gamma_N & -\epsilon_N & \zeta_N
\end{pmatrix}
\begin{pmatrix}
D_1^a \\
D_1^b \\
D_2^a \\
D_2^b \\
\vdots \\
\vdots \\
D_N^a \\
D_N^b \\
S
\end{pmatrix}
=
\begin{pmatrix}
0 \\
0 \\
0 \\
0 \\
0 \\
0 \\
\vdots \\
0 \\
0 \\
0
\end{pmatrix}. \tag{25}$$

Hence, the minimum non-zero solution of Eq. (25) is the ratio between each depth and the absolute scale value.

References

Bae S, Agarwala A, Durand F (2010) Computational rephotography. *ACM Transactions on Graphics* 29(3):24–1

Balntas V, Li S, Prisacariu V (2018) RelocNet: Continuous metric learning relocalisation using neural nets. In: *Proceedings of the European Conference on Computer Vision*, pp 751–767

Bay H, Tuytelaars T, Van Gool L (2006) Surf: Speeded up robust features. In: *Proceedings of the European Conference on Computer Vision*, Springer, pp 404–417

DeTone D, Malisiewicz T, Rabinovich A (2018) Superpoint: Self-supervised interest point detection and description. In: *Proceedings of the IEEE Conference on Computer Vision and Pattern Recognition Workshops*, pp 224–236

Dusmanu M, Rocco I, Pajdla T, Pollefeys M, Sivic J, Torii A, Sattler T (2019) D2-Net: A trainable cnn for joint description and detection of local features. In: *Proceedings of the IEEE Conference on Computer Vision and Pattern Recognition*, pp 8092–8101

Faugeras OD, Lustman F (1988) Motion and structure from motion in a piecewise planar environment. *International Journal of Pattern Recognition and Artificial Intelligence* 2(03):485–508

Feng W, Tian FP, Zhang Q, Zhang N, Wan L, Sun J (2015) Fine-grained change detection of misaligned scenes with varied illuminations. In: *Proceedings of the IEEE International Conference on Computer Vision*, pp 1260–1268

Feng W, Tian FP, Zhang Q, Sun J (2016) 6D dynamic camera relocalization from single reference image. In: *Proceedings of the IEEE Conference on Computer Vision and Pattern Recognition*, pp 4049–4057

Fischler MA, Bolles RC (1981) Random sample consensus: a paradigm for model fitting with applications to image analysis and automated cartography. *Communications of the ACM* 24(6):381–395

Goyette N, Jodoin PM, Porikli F, Konrad J, Ishwar P (2012) Changedetection. net: A new change detection benchmark dataset. In: *Proceedings of the IEEE Conference on Computer Vision and Pattern Recognition Workshop*, pp 1–8

Guggenheim D, Gore A, Bender L, Burns SZ, David L, Documentary GW (2006) *An inconvenient truth*. Paramount Classics Hollywood, CA

Guzman-Rivera A, Kohli P, Glocker B, Shotton J, Sharp T, Fitzgibbon A, Izadi S (2014) Multi-output learning for camera relocalization. In: *Proceedings of the IEEE conference on computer vision and pattern recognition*, pp 1114–1121

Hartley RI (1997) In defense of the eight-point algorithm. *IEEE Transactions on Pattern Analysis and Machine Intelligence* 19(6):580–593

He K, Gkioxari G, Dollár P, Girshick R (2017) Mask r-cnn. In: *Proceedings of the IEEE International Conference on Computer Vision*, pp 2961–2969

Jackway PT, Deriche M (1996) Scale-space properties of the multiscale morphological dilation-erosion. *IEEE Transactions on Pattern Analysis and Machine Intelligence* 18(1):38–51

Kendall A, Grimes M, Cipolla R (2015) PoseNet: A convolutional network for real-time 6-dof camera relocalization. In: *Proceedings of the IEEE International Conference on Computer Vision*, pp 2938–2946

Laskar Z, Melekhov I, Kalia S, Kannala J (2017) Camera relocalization by computing pairwise relative poses using convolutional neural network. In: *Proceedings of the IEEE International Conference on Computer Vision Workshops*, pp 929–938

Liu C, Kim K, Gu J, Furukawa Y, Kautz J (2019) Planercnn: 3d plane detection and reconstruction from a single image. In: *Proceedings of the IEEE Conference on Computer Vision and Pattern Recognition*, pp 4450–4459

Lowe DG (2004) Distinctive image features from scale-invariant keypoints. *International Journal of Computer Vision* 60(2):91–110

Maddalena L, Petrosino A (2012) The sobs algorithm: What are the limits? In: *Proceedings of the IEEE Conference on Computer Vision and Pattern Recognition Workshop*, pp

21–26

- Miao D, Tian FP, Feng W (2018) Active camera relocalization with rgbd camera from a single 2d image. In: IEEE International Conference on Acoustics, Speech and Signal Processing, IEEE, pp 1847–1851
- Mur-Artal R, Tardós JD (2017) Orb-slam2: An open-source slam system for monocular, stereo, and rgb-d cameras. *IEEE Transactions on Robotics* 33(5):1255–1262
- Nistér D (2004) An efficient solution to the five-point relative pose problem. *IEEE Transactions on Pattern Analysis and Machine Intelligence* 26(6):756–770
- Radenović F, Tolias G, Chum O (2018) Fine-tuning cnn image retrieval with no human annotation. *IEEE Transactions on Pattern Analysis and Machine Intelligence* 41(7):1655–1668
- Rublee E, Rabaud V, Konolige K, Bradski G (2011) Orb: An efficient alternative to sift or surf. In: Proceedings of the IEEE International conference on computer vision, pp 2564–2571
- Sarlin PE, Cadena C, Siegwart R, Dymczyk M (2019) From coarse to fine: Robust hierarchical localization at large scale. In: Proceedings of the IEEE Conference on Computer Vision and Pattern Recognition, pp 12716–12725
- Sattler T, Zhou Q, Pollefeys M, Leal-Taixe L (2019) Understanding the limitations of cnn-based absolute camera pose regression. In: Proceedings of the IEEE Conference on Computer Vision and Pattern Recognition, pp 3302–3312
- Shi YB, Tian FP, Miao D, Feng W (2018) Fast and reliable computational rephotography on mobile device. In: IEEE International Conference on Multimedia and Expo, IEEE, pp 1–6
- Shotton J, Glocker B, Zach C, Izadi S, Criminisi A, Fitzgibbon A (2013) Scene coordinate regression forests for camera relocalization in rgb-d images. In: Proceedings of the IEEE Conference on Computer Vision and Pattern Recognition, pp 2930–2937
- Staniforth S (2013) Historical perspectives on preventive conservation, vol 6. Getty Publications
- Tian FP, Feng W, Zhang Q, Wang X, Sun J, Loia V, Liu ZQ (2018) Active camera relocalization from a single reference image without hand-eye calibration. *IEEE Transactions on Pattern Analysis and Machine Intelligence* 41(12):2791–2806
- Ummenhofer B, Zhou H, Uhrig J, Mayer N, Ilg E, Dosovitskiy A, Brox T (2017) Demon: Depth and motion network for learning monocular stereo. In: Proceedings of the IEEE Conference on Computer Vision and Pattern Recognition, pp 5038–5047
- Wells II JE (2012) Western landscapes, western images: A rephotography of us highway 89. PhD thesis, Kansas State University
- Yi KM, Trulls E, Lepetit V, Fua P (2016) Lift: Learned invariant feature transform. In: Proceedings of the European Conference on Computer Vision, Springer, pp 467–483
- Zhang Q, Feng W, Wan L, Tian FP, Tan P (2018) Active recurrence of lighting condition for fine-grained change detection. In: International Joint Conference on Artificial Intelligence, pp 4972–4978
- Zhou F, De la Torre F (2013) Deformable graph matching. In: Proceedings of the IEEE Conference on Computer Vision and Pattern Recognition, pp 2922–2929
- Zhou Q, Sattler T, Pollefeys M, Leal-Taixe L (2020) To learn or not to learn: Visual localization from essential matrices. In: IEEE International Conference on Robotics and Automation, IEEE, pp 3319–3326